nature catalysis

ARTICLES

https://doi.org/10.1038/s41929-018-0201-7

Evidence for product-specific active sites on oxide-derived Cu catalysts for electrochemical CO_2 reduction

Yanwei Lum [1,2] and Joel W. Ager [1,2*]

Carbon dioxide electroreduction in aqueous media using Cu catalysts can generate many different C_2 and C_3 products, which leads to the question whether all products are generated from the same types of active sites or if product-specific active sites are responsible for certain products. Here, by reducing mixtures of ^{13}CO and $^{12}CO_2$, we show that oxide-derived Cu catalysts have three different types of active sites for C–C coupled products, one that produces ethanol and acetate, another that produces ethylene and yet another that produces 1-propanol. In contrast, we do not find evidence of product-specific sites on polycrystalline Cu and oriented (100) and (111) Cu surfaces. Analysis of the isotopic composition of the products leads to the prediction that the adsorption energy of *COOH (the product of the first step of CO_2 reduction) may be a descriptor for the product selectivity of a given active site. These new insights should enable highly selective catalysts to be developed.

The past few decades alone have seen large increases in atmospheric CO_2 concentrations, mainly due to humankind's consumption of fossil fuels for energy[1]. It has been projected that global energy consumption will continue to rise, leading to a tripling of CO_2 emissions by 2040[1]. There is therefore an urgent need to develop technologies capable of efficiently harvesting and storing renewable energy to reduce our dependence on fossil fuels[2].

Electrochemical CO_2 reduction (CO_2R) in aqueous media presents an attractive and viable strategy to reduce carbon emissions by directly converting CO_2 into valuable hydrocarbons and oxygenates such as ethylene and ethanol[3,4]. To date, Cu remains the most promising catalyst capable of driving this conversion process at reasonable current densities[5,6]. Although methane, ethylene and ethanol are the major products, up to 18 different possible products can be produced[7–9]. It is commonly accepted that, except for formate, CO_2R on Cu is initiated by reducing CO_2 to adsorbed CO (*CO)[10–13]. Further protonation of *CO results in methane and methanol formation (C_1 pathway) or *CO can couple with another *CO (C–C coupling), which leads to C_2 and C_3 products, such as ethylene and 1-propanol[14–16]. However, although there have been intriguing reports of selective ethylene production under a certain range of conditions and at high current densities[17,18], it has been experimentally difficult to control selectivity to a given C_2 or C_3 product. To improve the catalyst performance and selectivity further, it is crucial to first identify and understand the nature of the active sites that are present on Cu electrocatalysts. A related and important question is whether all the products are produced from the same active sites or if specific active sites generate a given product. In other words, are there product-specific active sites that mostly generate only one product?

We reasoned that it would be possible to answer these critical questions by performing an electroreduction of a mixture of ^{13}CO and $^{12}CO_2$. To explain our rationale, consider a hypothetical catalyst that possesses only two types of active sites for C_2 production (Fig. 1). We assume that one site (A) is selective for ethylene whereas the other (B) is selective for ethanol. As their catalytic properties are different, we would expect that the adsorption energies of the intermediates, often used as a descriptor for catalytic activity[19–21], should also be different on the two sites. Due to the difference in intermediate adsorption energies, we would naturally expect that the turnover frequencies for generating these intermediates will be different. As a specific example, the rate of the initial step of CO_2R, converting CO_2 to *CO, will be different on the two sites. As a result, if we were to reduce a mixture of ^{13}CO and $^{12}CO_2$, the turnover frequency for $^{12}CO_2$ reduction to $^{*12}CO$ should be active-site dependent, which results in sites A and B having different probabilities of being occupied by $^{*12}CO$ versus $^{*13}CO$. In this case, we assume that the turnover frequency of $^{12}CO_2$ reduction to $^{*12}CO$ is higher for site B, which leads to a higher (lower) probability of $^{*12}CO$ ($^{*13}CO$) on this site.

In the next electrocatalytic step, C–C coupling between the *CO on the sites, followed by a series of proton-coupled electron transfers and dehydration steps[16,22–24], results in the formation of ethylene (for site A) and ethanol (for site B). Crucially, the isotopic composition of the products will be different: in this hypothetical case, ethylene will have more ^{13}C than ethanol. More generally, this analysis shows that if a mixture of ^{13}CO and $^{12}CO_2$ is reduced, the isotopic composition of the C–C coupled products will serve as a fingerprint of the active sites that produced them. That is, if two C–C coupled products have different isotopic compositions, then they have been produced by different types of active sites. However, if the catalyst does not have product specific active sites, then all the products should have similar isotopic compositions.

In this work, we apply this isotope labelling concept to analyse the active sites on oxide-derived Cu catalysts. Such catalysts are typically prepared by oxidation of a Cu foil or film, followed by reduction to its metallic state[25–29]. This class of catalysts, originally reported by Kanan and co-workers, is of significant interest because they show dramatically reduced overpotentials for the reduction of CO to oxygenate products (for example, ethanol) with high Faradaic efficiencies[27,30]. Furthermore, work from many research groups has shown that these catalysts exhibit an enhanced selectivity for reducing CO_2 to C_2 and C_3 products, but suppress the formation of C_1 products[25,26,28,31–33].

[1]Joint Center for Artificial Photosynthesis and Materials Sciences Division, Lawrence Berkeley National Laboratory, Berkeley, CA, USA. [2]Department of Materials Science and Engineering, University of California, Berkeley, CA, USA. *e-mail: jwager@lbl.gov

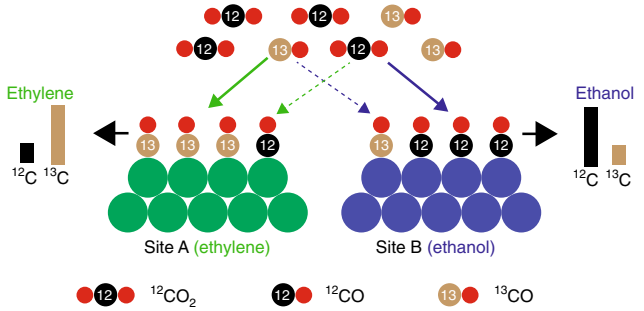

Fig. 1 | Hypothetical scenario in which the reduction of a mixture of ^{13}CO and $^{12}CO_2$ is carried out on a catalyst with two types of active sites, A and B. Site A favours ethylene formation (green), whereas site B favours ethanol formation (blue). It is assumed that the turnover frequency of $^{12}CO_2$ reduction to $*^{12}CO$ is higher for ethanol-selective sites, which leads to a higher probability of $*^{12}CO$ on site B. This results in ethylene having more ^{13}C compared to ethanol.

A number of studies aimed to identify the active sites responsible for the unique catalytic properties of oxide-derived Cu. Chorkendorff and co-workers used temperature programmed desorption to detect strong CO binding sites that are not present on polycrystalline Cu (ref. [34]). They posited that these strong binding sites could be the grain boundaries observed in their oxide-derived Cu catalysts. In related work, Kanan and co-workers demonstrated that grain boundaries are the active sites for the reduction of CO to C_2 and C_3 products[34,35]. However, it is not known whether all the grain boundaries are active or if only those with specific structures are responsible for generating most of the products.

The objective of this work is to determine if product-specific active sites are responsible for the superior C_2 and C_3 selectivity of oxide-derived Cu. Evidence of product-specific sites will motivate future studies to understand how each of these different active sites work and to develop methods that build specific types of product-specific sites into a single structure, both of which could lead to CO_2R catalysts with a greatly improved product selectivity. Indeed, we discovered that oxide-derived Cu has at least three types of active sites which selectively produce ethylene, ethanol/acetate and 1-propanol, respectively. In contrast, polycrystalline Cu and Cu(100)- and Cu(111)-oriented surfaces do not appear to have product-specific active sites.

Results

Reduction of ^{13}CO and $^{12}CO_2$ mixtures. Due to the large differences in the aqueous solubility between ^{13}CO (1 mM) and $^{12}CO_2$ (33.4 mM), selecting their ratio to achieve a given ^{12}CO:^{13}CO surface coverage merits some discussion. Based on calculations and experiments (Supplementary Figs. 1 and 2), we estimated that a 70:30 ratio of ^{13}CO to $^{12}CO_2$ would allow similar rates of $*^{13}CO$ and $*^{12}CO$ formation to occur. Oxide-derived Cu catalysts were prepared according to procedures described by Kanan and co-workers[27] (Supplementary Figs. 3–5). Polycrystalline Cu was prepared by electropolishing Cu foil and the oriented surfaces of Cu(100) and Cu(111) were fabricated using procedures developed by Jaramillo and co-workers[36]. Natural abundance CO_2R in 0.1 M $KHCO_3$ with these catalysts qualitatively reproduced previously reported results (Supplementary Figs. 6 and 8–10). Natural abundance CO reduction in 0.1 M KOH (Supplementary Fig. 7) confirmed that our oxide-derived Cu catalysts performed similarly to those reported by Kanan and co-workers[27]. Gas chromatography–mass spectrometry (GCMS) and ^{13}C nuclear magnetic resonance (NMR) spectroscopy were employed to determine the isotopic composition of the gas and liquid products (Methods, Supplementary Figs. 11–23 and Supplementary Tables 1–8 give details). For experimental validation, we reduced $^{13}CO/^{12}CO$ in ratios of 1:3, 1:1 and 3:1 on the oxide-derived Cu catalyst and observed the expected statistical isotope compositions and distributions (Supplementary Tables 9–14 give details). Throughout this work, we refer to the isotopic composition as the fraction of ^{13}C in the product. Additionally, the $^{12}C/^{13}C$ distribution, for example, of ethylene, refers to the fractions of the three possible product variants: $^{12}CH_2{}^{12}CH_2$, $^{12}CH_2{}^{13}CH_2$ and $^{13}CH_2{}^{13}CH_2$.

Confident of our experimental and analytical methods, we proceeded to carry out the reduction of the 70:30 $^{13}CO/^{12}CO_2$ gas mixture with the oxide-derived Cu catalyst. Figure 2a shows the isotopic compositions of ethylene, ethanol, acetate and 1-propanol produced by oxide-derived Cu at four different applied potentials in 0.1 M $KHCO_3$ electrolyte. There are a number of striking findings. First, regardless of the applied potential, the isotopic compositions (^{13}C fraction) of ethanol and acetate are identical, which strongly suggests that these products are generated from the same active sites. Second, it also appears that ethylene is produced from a different set of active sites, as evidenced by its consistently higher ^{13}C fraction as compared to those of ethanol/acetate. It is also observed that the ^{13}C fraction of ethylene changes more strongly with potential compared to the other products. Finally, 1-propanol also has a ^{13}C fraction that appears distinct from either that of ethylene or of ethanol/acetate, which means that this product is generated by yet another set of active sites.

A more detailed analysis of the isotopic compositions provides information on the properties of the different active sites. For these four products, it appears that the ^{13}C fraction decreases with a more negative applied overpotential. This is probably because at more negative applied overpotentials, the turnover frequency for converting $^{12}CO_2$ into $*^{12}CO$ on all the active sites should increase, and thereby increase the probability of having a $*^{12}CO$ versus $*^{13}CO$ on all the active sites. As the ^{13}C fraction of ethanol/acetate is consistently lower than that of the other products, the active sites that generate these products must have a higher probability of containing a $*^{12}CO$. Therefore, the active sites that generate ethanol/acetate should have catalytic properties such that they are also able to drive $^{12}CO_2$ into $*^{12}CO$ with a turnover frequency larger than that of the ethylene active sites or 1-propanol active sites. Finally, the stronger potential dependence of the ^{13}C fraction of ethylene implies that the turnover frequency of $^{12}CO_2$ to $*^{12}CO$ should also have the largest potential dependence compared to the other active sites.

The notion that ethylene and ethanol/acetate are formed on product-specific active sites on oxide-derived Cu is further supported by the binomial nature of their $^{12}C/^{13}C$ distributions. The $^{12}C/^{13}C$ distributions for these products at −0.72 V are shown in Fig. 2b–d (Supplementary Fig. 27 gives the $^{12}C/^{13}C$ distributions at other potentials). As a comparison, the predicted binomial distributions for each product are shown as well in each of the figures (calculated based on the isotopic composition; Supplementary Tables 3–5 gives more details). If products were generated from multiple active sites that are not product specific, the $^{12}C/^{13}C$ distribution would be a superposition of multiple binomial distributions, which would result in deviations from a true binomial distribution. Another observation is that the observed $^{12}C/^{13}C$ distributions of ethanol and acetate (Fig. 2c,d) appear to be identical, which is further evidence that these products are generated from the same active sites.

We developed a multisite kinetic model that predicts product isotopic distributions as a function of the selectivity of the active sites, the $*^{13}CO$:$*^{12}CO$ ratio at a given site and the number of active sites of a given type and their turnover frequency (Supplementary Figs. 28–30 and Supplementary Tables 15–17 give model details). The model allows consideration of the effects that would cause the $*^{13}CO$:$*^{12}CO$ ratio to be similar for all sites, such as the surface diffusion of *CO and/or desorption and re-adsorption events. Clearly,

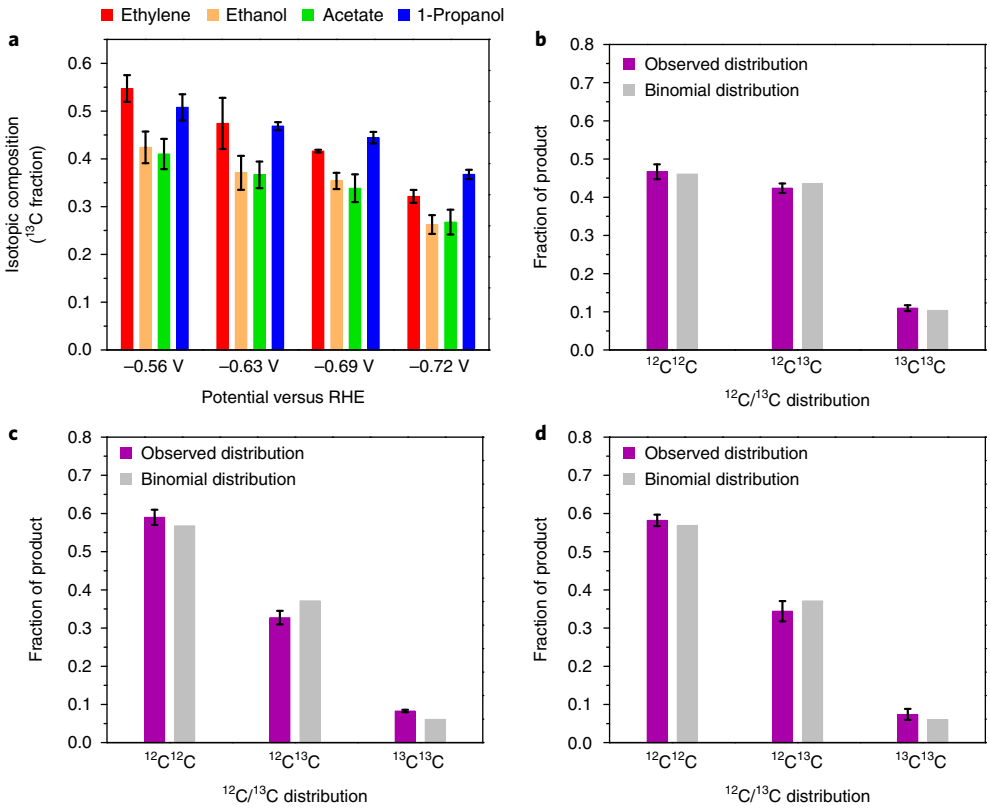

Fig. 2 | Isotopic compositions and $^{12}C/^{13}C$ distributions of products generated by oxide-derived Cu. a, Isotopic composition of ethylene, ethanol, acetate and 1-propanol produced by the reduction of the $^{13}CO/^{12}CO_2$ gas mixture with oxide-derived Cu at four different potentials. **b**–**d**, $^{12}C/^{13}C$ distributions of ethylene (**b**), ethanol (**c**) and acetate (**d**) at −0.72 V versus RHE. Supplementary Fig. 27 gives the $^{12}C/^{13}C$ distributions at other potentials. All the distributions appear to be binomial, comparisons with the predicted binomial distribution based on the isotopic composition (calculation details in Supplementary Tables 3–5). Faradaic efficiency and current density data are shown in Supplementary Fig. 24. Catalyst stability data are shown in Supplementary Figs. 25 and 26. Error bars correspond to the s.d. of three independent measurements.

that we see differences in isotopic composition between the products means that the reduction of CO to products necessarily outcompetes these isotopic scrambling effects. The model also shows that the sites must be substantially selective to observe both differences in ^{13}C composition and a $^{12}C/^{13}C$ distribution that does not differ significantly from a binomial distribution.

Next, to determine if the existence of product-specific active sites is a feature of Cu electrocatalysts in general, we performed the reduction of the $^{13}CO/^{12}CO_2$ gas mixture with polycrystalline Cu and Cu(111)- and Cu(100)-oriented surfaces. Figure 3a shows the isotopic composition of the products at −0.9 V versus a reversible hydrogen electrode (RHE). In some cases, the isotopic compositions of acetate and 1-propanol could not be determined accurately as their formation rates were too low. In contrast to the case for oxide-derived Cu, we observe that the isotopic composition for the products generated are very similar, which means that these catalysts do not have product-specific active sites. In Fig. 3b,c, the $^{12}C/^{13}C$ distributions of ethylene and ethanol generated by polycrystalline Cu appear to deviate slightly from the predicted binomial distribution. This might suggest that polycrystalline Cu may have multiple active sites that are not product specific. In this scenario, each type of active site might have a different probability of $^{*12}CO$ versus $^{*13}CO$, which results in the $^{12}C/^{13}C$ distributions of the products being a superposition of a few binomial distributions. To ensure that the similar isotopic compositions of the products was not just a coincidence that happens only at −0.9 V versus RHE, we tested Cu(100) at −0.8 V versus RHE. As expected, all the products possess similar isotopic compositions, albeit with higher ^{13}C fractions due to the lower overpotential that was applied (Fig. 3d).

Control experiments. We performed a series of control experiments to rule out local pH, surface area/roughness and catalyst morphology effects as possible explanations for our striking findings on oxide-derived Cu. First, during CO_2R the local pH of the surface rises above that of the bulk pH because protons from water are consumed to drive the reduction of CO_2 and hydrogen evolution[3,37]. This rise in local pH of the catalyst surface during CO_2R has been observed to suppress C_1 formation and enhance C–C coupling, and thereby increase selectivity towards C_2 products[17,25,29,38]. For high surface area catalysts, such as oxide-derived Cu, the rise in local pH is larger as compared to that in planar Cu electrodes due to the larger geometric current densities[26]. Therefore, to minimize local pH changes, we reduced the $^{13}CO/^{12}CO_2$ gas mixture with oxide-derived Cu in a 0.1 M phosphate buffer (pH 7.2) at a potential of −0.63 V. Such a buffer has been previously shown to significantly mitigate rises in local pH[3,28,39]. Figure 4a shows that the isotopic compositions of ethylene, ethanol/acetate and 1-propanol remain distinct from each other in phosphate buffer, which allows us to rule out local pH effects as a possible explanation for our results.

To rule out surface area and/or roughness effects, we tested Cu catalysts prepared by electrodeposition. This process generates catalysts with high surface areas but does not involve an oxidized Cu intermediate (details in Methods). Two catalysts were prepared: electrodeposited Cu A, which has a comparable roughness factor to oxide-derived Cu (Supplementary Table 18), and electrodeposited Cu B, which has a smaller roughness factor (scanning electron microscopy (SEM) images in Fig. 4b,c insets). Figure 4b shows that products of $^{13}CO/^{12}CO_2$ reduction at −0.67 V versus RHE on electrodeposited Cu A have similar isotopic compositions. Similar

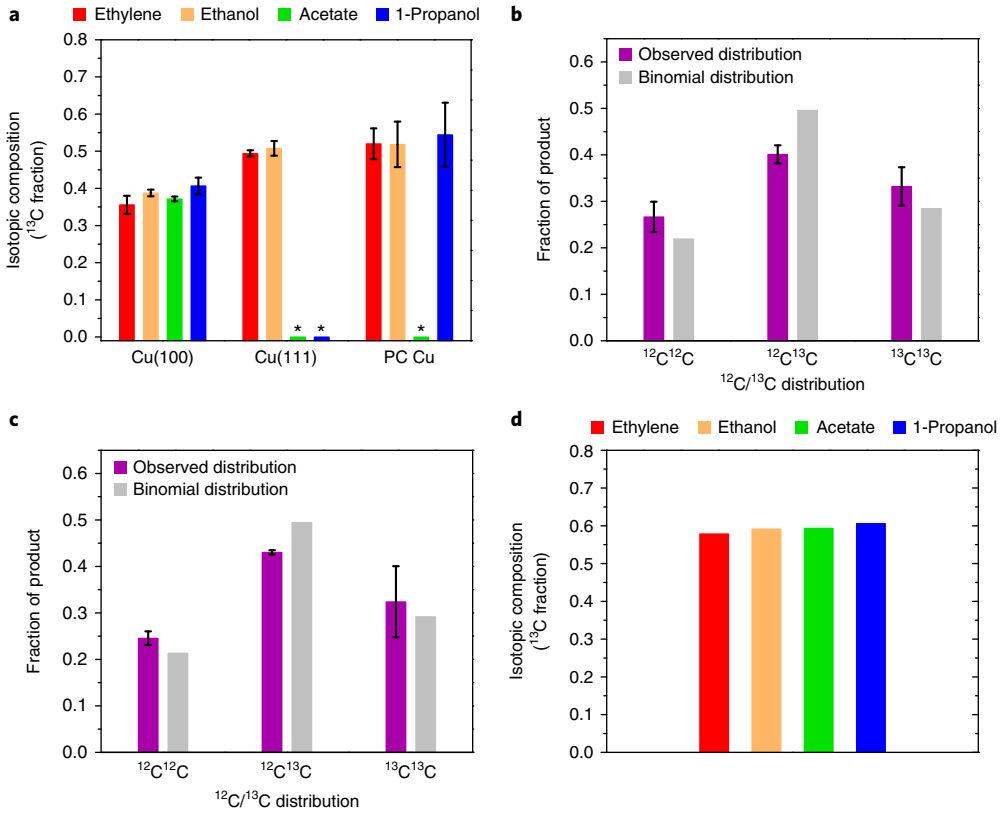

Fig. 3 | Isotopic compositions and $^{12}C/^{13}C$ distributions of products generated by Cu(111)- and Cu(100)-oriented surfaces and polycrystalline Cu. **a**, Isotopic compositions of products generated by Cu(100), Cu(111) and polycrystalline Cu at −0.9 V versus RHE. The stars in the figure indicate that the isotopic composition could not be determined accurately. **b**,**c**, Observed and predicted binomial $^{12}C/^{13}C$ distributions of ethylene (**b**) and ethanol (**c**) for polycrystalline Cu. **d**, Isotopic compositions of products generated by Cu(100) at −0.8 V versus RHE. $^{12}C/^{13}C$ distributions for Cu(100) and Cu(111) are shown in Supplementary Fig. 31. Catalysis data are shown in Supplementary Fig. 32. Error bars correspond to the s.d. of three independent measurements.

results were also obtained on electrodeposited Cu B, which was tested at −0.87 V versus RHE (Fig. 4c). As we did not observe differences in isotopic composition between the products, which we did with oxide-derived Cu, we ruled out surface area and roughness as a possible explanation of our results. Additionally, it is apparent that such catalyst preparation methods do not result in creation of product-specific sites.

Finally, catalyst morphology has been shown to be important in determining the selectivity of Cu catalysts[40]. To explore this effect, we synthesized an oxide-derived Cu catalyst with a distinctly different morphology from oxide-derived Cu. Oxide-derived Cu nanowire catalysts were synthesized according to the procedure described by Smith and co-workers[25] with some modifications (Methods gives details and an SEM image is shown in Fig. 4d (inset)). Figure 4d shows that the isotopic compositions of ethylene, ethanol/acetate and 1-propanol obtained by the reduction of $^{13}CO/^{12}CO_2$ at −0.62 V versus RHE are also different from each other. This means that, as for oxide-derived Cu, oxide-derived Cu nanowires also possesses product-specific active sites. Similarly, we can rule out the possibility that the observed differences in isotopic composition are a result of morphology effects.

Mechanistic insights. Besides the finding that the active sites on oxide-derived Cu are product specific, several other mechanistic insights can be gained from this work. To explain the oxygenate generation on Cu-based catalysts from CO_2R, several research groups proposed that mobile non-adsorbed CO can undergo an insertion reaction with surface bound $*CH_2$ species to form a $*COCH_2$ intermediate[41–43]. Further reduction of $*COCH_2$ would lead to the formation of ethanol and possibly 1-propanol as well[13]. Also, Meyer and co-workers further proposed that this $*COCH_2$ intermediate could lead to the formation of acetate[42]. This type of CO insertion mechanism was first proposed by Hori and co-workers, using an analogy to Fischer–Tropsch catalysis and here we refer to it as the CO insertion mechanism[13].

Using our approach, evidence of a CO insertion mechanism could be observed in two ways. First, according to the mechanism proposed by Hori, $^{12}CO_2$ would reduce to surface-bound $*^{12}CO$ and subsequently to $*^{12}CH_2$. Labelled CO insertion would yield a $*^{13}CO^{12}CH_2$ intermediate, which would then reduce to form ethanol, 1-propanol or acetate. Importantly, this mechanism predicts that the ^{13}C should be in the α carbon position ($-CH_2OH$) rather than the β carbon position ($-CH_3$). Similarly, for 1-propanol, ^{13}C should be in the α position ($-CH_2OH$) rather than the β ($-CH_2-$) or γ ($-CH_3$) positions. As for acetate, ^{13}C should be in the carboxyl group ($-COO^-$) rather than the α position ($-CH_3$). However, ^{13}C NMR spectroscopy reveals no such preference for ^{13}C to be in any of the positions relative to another (more details in Supplementary Figs. 39–44). Second, CO insertion would not produce a binomial distribution of ^{12}C and ^{13}C in the C_2 products but rather a distribution with enhanced $^{12}C^{13}C$ formation, as compared to the $^{12}C^{12}C$ or $^{13}C^{13}C$. The $^{12}C/^{13}C$ distributions of ethanol or acetate do not appear to display a strong bias for the formation of the $^{12}C^{13}C$ product (Figs. 2 and 3 and Supplementary Figs. 27 and 31). Thus, we conclude that the CO insertion mechanism does not occur in the catalyst systems in this study.

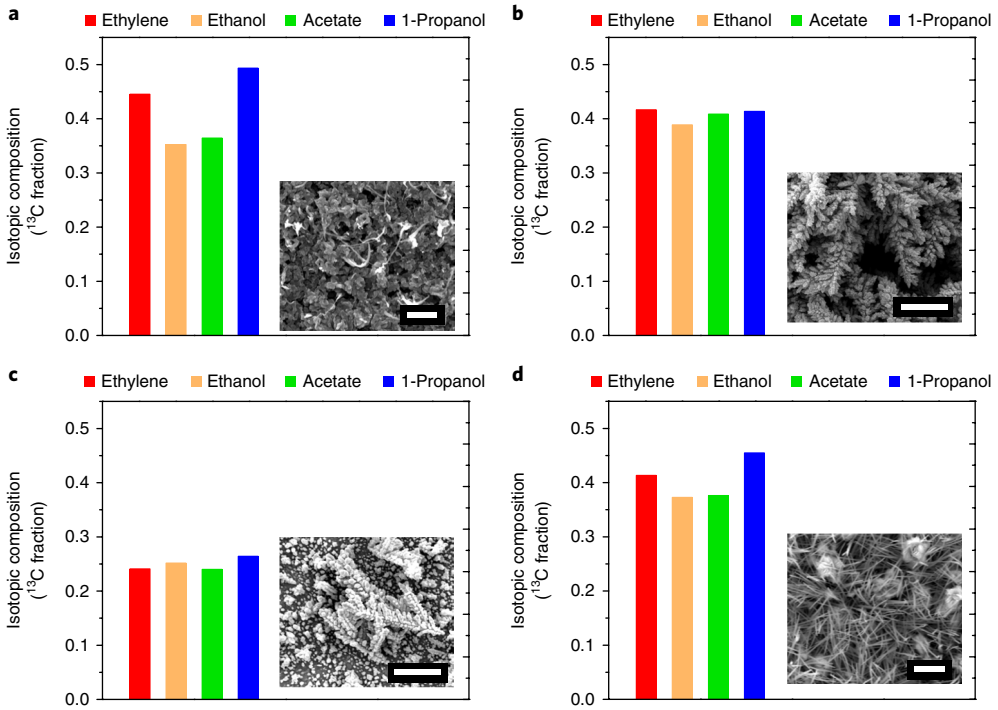

Fig. 4 | Isotopic compositions of products generated in control experiments. a, Oxide-derived Cu in 0.1 M phosphate buffer at a potential of −0.63 V versus RHE with an SEM image (inset). Scale bar, 1 μm. **b**, Electrodeposited Cu A at −0.67 V in 0.1 M $KHCO_3$ with an SEM image (inset). Scale bar, 4 μm. **c**, Electrodeposited Cu B at −0.87 V in 0.1 M $KHCO_3$ with an SEM image (inset). Scale bar, 4 μm. **d**, Oxide-derived Cu nanowires at −0.62 V in 0.1 M $KHCO_3$ with an SEM image (inset). Scale bar, 5 μm. Catalysis data are shown in Supplementary Fig. 37. More SEM images are available in Supplementary Figs. 34–36.

Another interesting experimental observation is that ethanol and acetate are generated from the same active sites on oxide-derived Cu. This means that these products are likely to be linked mechanistically and thus share the same selectivity-determining intermediates and/or steps. Indeed, ethanol and acetate have been linked closely together in previous reports. Kanan and co-workers observed substantial acetate formation at high pH during CO reduction on oxide-derived Cu, which they ascribed to the attack of carbonyl-containing intermediates by OH^- (ref. [27]). As the increased acetate formation at high pH was accompanied by a decrease in ethanol, it can be inferred that the products share a common intermediate. As another example, Koper and co-workers proposed that Cannizzaro disproportionation of acetaldehyde generates both acetate and ethanol simultaneously[44]. However, our observation that ethylene and 1-propanol are generated from different sites suggests that these products do not share common selectivity-determining intermediates and/or steps and branch early on after C–C coupling from the ethanol/acetate pathway. Additionally, our results do not support the mechanism proposed by Head-Gordon and co-workers, which places acetate on the ethylene pathway rather than on the ethanol pathway[12].

Additionally, our experimental observations on oxide-derived Cu may also be rationalized from the point of view of scaling relations. In CO_2R, intermediates bind to the surface through the C and/or the O atom[10,12,24,45]. From scaling relations, intermediates that bind through the C atom are expected to have adsorption energies that are linearly related to each other, with the same rationale applying to intermediates that bind through the O atom. For ethylene-selective sites, the adsorption energies of intermediates must all be shifted in a way such that after C–C coupling, the formation of the ethylene intermediate is by far the most kinetically favourable compared to that of the ethanol/acetate or 1-propanol intermediates. However, shifting the adsorption energies of intermediates in a different way could result in favouring the formation of the ethanol/acetate intermediate or the 1-propanol intermediate. Recalling the identification, by Chorkendorff and co-workers[34], of a range of strong CO adsorption sites on oxide-derived Cu not present on polycrystalline Cu, we find it possible that these strong CO adsorption sites are associated with the product-specific sites that we have discovered. Further we posit that these sites have specific combinations of C and O adsorption energies that enable them to become product specific. Kanan and co-workers showed that grain boundaries are the active sites on oxide-derived Cu for the reduction of CO to C_2 and C_3 products[34,35]. We therefore think it possible that the structure of each product-specific active site may be a specific type of grain boundary termination.

Another consequence of scaling relations is its effect on the formation of $*^{12}CO$ from $^{12}CO_2$. Theoretical studies predict that the rate-limiting step of this reaction is the formation of *COOH from $*CO_2$ (refs [11,15,46]). As we have consistently observed that ethanol/acetate have the highest ^{12}C fractions (Fig. 2a), their active sites should have the highest $^{12}CO_2$ to $*^{12}CO$ turnover frequencies. We thus posit that, due to scaling relations, enhancing the formation of the $*^{12}COOH$ intermediate by tuning the catalyst adsorption energies also enhances the formation of the ethanol/acetate intermediate. Additionally, ethylene- and 1-propanol-selective sites should have different *COOH adsorption energies to those of ethanol/acetate-selective sites because their ^{13}C fractions depend differently on the applied potential (Fig. 2a). This probably means that *COOH adsorption energies may be a descriptor for the product selectivity of an active site. Thus, turnover frequencies for $^{12}CO_2$ and $*^{12}CO$ are active-site dependent, so each site has a different probability of $*^{12}CO$ versus $*^{13}CO$. This gives rise to the different product isotopic compositions we have observed.

Finally, a theory paper published by Goddard and co-workers could possibly offer some insight on our results and serve as a

starting point towards identifying the different active sites we have observed[47]. Using molecular dynamics, they randomly generated sites on Cu nanoparticles with different atomic configurations. Approximately 9% of these generated sites had a larger CO binding energy than that of Cu(211). This seems to be consistent with the temperature-programmed desorption study of Chorkendorff and co-workers in which they found stronger CO binding sites on oxide-derived Cu that are not present on polycrystalline Cu (ref. [34]). Among the strong CO binding sites, the theoretical study identified two atomic configurations that were proposed to be active for C–C coupling. Relating these findings to our experimental work, it is conceivable that some of the sites studied by Goddard and co-workers could also be present on the oxide-derived Cu surface. It is possible that the differences in CO binding energy for different surface configurations could be used to identify product-selective sites for C_2 and C_3, although more precise knowledge of the selectivity-determining steps is required.

Conclusions

In summary, we have shown via isotope labelling that oxide-derived Cu has product-specific active sites for the CO_2R reaction, with one set of active sites generating ethylene, another ethanol/acetate and yet another 1-propanol. We reason that, due to scaling relations, the rate of *COOH formation (intermediate to *CO) should be different for each type of active site. This means that each active site has a different probability of $*^{12}CO$ versus $*^{13}CO$ and, as a result, products generated from different sites possess different isotopic compositions. In contrast, by performing similar experiments on polycrystalline Cu, Cu(100) and Cu(111), we showed that these have sites that produces a mixture of C–C coupled products. Finally, our finding that active sites on oxide-derived Cu are product specific should motivate future work to understand these sites as well as ways to engineer specific types of sites into a single structure, and thereby create catalysts with very high product selectivities.

Methods

Materials. Potassium carbonate (99.995% metal basis), potassium hydroxide (99.99% metal basis), ^{13}C carbon monoxide (<5 atom% ^{18}O, 99 atom% ^{13}C), nitric acid (70%), hydrochloric acid (37%), potassium phosphate monobasic (99.99% metal basis) and potassium phosphate dibasic (99.95% metal basis) were purchased from Sigma-Aldrich. Copper foil (0.1 mm thick, 99.9999%) and glassy carbon plates were purchased from Alfa Aesar. Selemion AMV anionic exchange membranes were purchased from Asahi Glass Co. Ltd. Si wafers of various orientations were purchased from UniversityWafer Inc. The copper sputtering target (99.999%) was purchased from Kurt J. Lesker Company. All the chemicals were used without further purification. Carbon dioxide (99.995%), nitrogen (99.999%), argon (99.999%) and hydrogen (99.999%) were purchased from Praxair. Natural abundance carbon monoxide (99.999% research purity) was purchased from Matheson Tri-gas Inc. Hydrogen, argon, nitrogen and carbon dioxide gas purifiers purchased from Valco Instruments Co. Inc. were used on the gas feeds to the electrochemical cell and gas chromatograph. Deionized (18.2 MΩ) water was produced by a Millipore system and used for the electrolyte preparation.

Preparation of polycrystalline Cu. Cu foil was cut into 2 cm by 2 cm square pieces and then electropolished at a potential of 2 V versus the counter electrode for a period of 5 min. The counter electrode used was another Cu foil of larger dimensions (5 cm by 5 cm).

Preparation of oxide-derived Cu. Oxide-derived Cu was prepared according to the procedure developed by Kanan and co-workers[27]. Cu foil was first cut into 2 cm by 2 cm square pieces and then electropolished at a potential of 2 V versus the counter electrode for a period of 5 min. The counter electrode used was another Cu foil of larger dimensions (5 cm by 5 cm). To oxidize the surface, the Cu foil was thermally annealed in air using a muffle furnace at a temperature of 500 °C for 1 h. The muffle furnace was then allowed to cool to room temperature before the oxidized Cu foils were removed.

Preparation of oriented Cu surfaces. Cu(100) and Cu(111) oriented surfaces were prepared according to similar procedures to those described by Jaramillo and co-workers[36]. Si wafers with different orientations were used as the growth substrates to facilitate the epitaxial growth of Cu. Cu films grown on Si(100) and Si(110) wafers yield Cu orientations of (100) and (111), respectively. The native oxide on the Si wafers was first removed via a HF etch and subsequent growth of the films was carried out using sputtering with an AJA International ATC Orion 5 sputtering system. In all cases, the thicknesses of the Cu films were controlled at 200 nm thick using a quartz crystal monitor. Samples were kept in a N_2-filled glove box when not in use to minimize oxidation in ambient air. The orientations were also confirmed according to similar procedures reported by Koper and co-workers[48] as well as Yeo and co-workers[32]. Briefly, this was accomplished with cyclic voltammetry in Ar-sparged 0.1 M KOH solution in the potential range of −1.3 V to −0.45 V versus Ag/AgCl at a rate of 120 mV s^{-1}. The OH^- adsorption and desorption peaks are unique and depend on the Cu surface and thus may be used to identify and confirm its orientation. Cyclic voltammetry was also carried out after CO reduction to confirm that loss of the surface orientation did not occur (Supplementary Fig. 33).

Preparation of oxide-derived Cu nanowires. Oxide-derived nanowires were prepared according to the method described by Smith and co-workers, with some modifications[25]. First, Cu foil was first cut into 2 cm by 2 cm square pieces and then electropolished at a potential of 2 V versus the counter electrode for a period of 5 min. The counter electrode used was another Cu foil of larger dimensions (5 cm by 5 cm). The Cu foil was then immersed for 10 min into an aqueous solution that contained 0.133 M $(NH_4)_2S_2O_8$ and 2.667 M NaOH, which resulted in the growth of $Cu(OH)_2$ nanowires on the surface. The foil was then thermally annealed in air using a muffle furnace at a temperature of 500 °C for 30 min to convert $Cu(OH)_2$ into CuO. The muffle furnace was then allowed to cool to room temperature before the Cu foils were removed.

Preparation of electrodeposited Cu. Electrodeposited Cu A and Cu B were prepared by the electrodeposition of Cu onto an electropolished Cu foil using a solution that contained 0.1 M $CuSO_4$ adjusted to pH 1 using concentrated H_2SO_4. A constant cathodic current density of −400 mA cm^{-2} was applied for 8 min for electrodeposited Cu A and only 2 min for electrodeposited Cu B. Such a procedure results in a dendritic, porous structure with a high surface area with a roughness factor that increases with increasing deposition time.

Materials characterization and electroactive surface area measurements. SEM images were taken on a FEI Quanta 200 FEG SEM using an accelerating voltage of 15 kV. X-ray diffraction patterns were obtained using a Rigaku Smartlab X-ray diffractometer.

Electroactive surface area measurements were performed according to procedures described by Nilsson and co-workers[33]. These measurements were performed in the same electrochemical cell as that for electrolysis experiments. The electrolyte used was 0.1 M $KHCO_3$ and cyclic voltammetry was carried out in a region where Faradaic processes do not occur. This was carried out with various scan rates and the geometric current density was plotted versus the scan rate. The slope of this graph is equal to the double layer capacitance.

Electrochemical measurements. For all electrochemical measurements described in this work, a Biologic SP-300 potentiostat was used. CO reduction was carried out using a custom-made electrochemical cell made of PEEK and fitted with Teflon O rings for chemical inertness and durability. In this cell, the working and counter electrodes were both constrained to be 1 cm^2 and to sit parallel to each other to ensure a uniform potential distribution across the working electrode surface. In all the electrochemical CO_2/CO reduction experiments, glassy carbon was used as the counter electrode (anode) instead of Pt due to concerns regarding Pt dissolution[49]. To ensure that the electrolyte remained saturated with $^{12}CO_2$ and ^{13}CO throughout electrolysis, these gases were continuously introduced into the electrochemical cell at a rate of 1.5 and 3.5 sccm, respectively, using mass-flow controllers. A custom-made glass frit fabricated by Adams & Chittenden Scientific Glass was used to disperse the gas into the electrolyte as well as provide adequate convection in the electrochemical cell[50]. Before carrying out bulk electrolysis experiments, the gas mixture was allowed to flow through the electrolyte in the cathode chamber for at least 15 min to ensure that the electrolyte was saturated. To separate the electrolyte in the cathode and anode chambers, a Selemion AMV anion exchange membrane was employed. Before use, the membrane was carefully rinsed with deionized water. The electrolyte volume used in both the cathode and anode was 1.8 ml. Before use in experiments, the electrochemical cell was sonicated in 20 wt% nitric acid for 1 h. All bulk electrolysis experiments were conducted for 70 min. A leak-free Ag/AgCl electrode from Innovative Instruments Inc. was employed as a reference electrode. The accuracy of this reference electrode was ensured periodically by comparison with a custom-made RHE. To convert potentials versus Ag/AgCl to the RHE scale, we used the equation:

$$E\ (\text{versus RHE}) = E\ (\text{versus Ag/AgCl}) + 0.197\ \text{V} + 0.0591\ \text{pH} \quad (1)$$

After saturation of the electrolyte with the gas mixture, the solution resistance was determined using potentiostatic electrochemical impedance spectroscopy, scanning through a frequency range of 1 MHz to 10 Hz. Then, 85% of the solution resistance was compensated using the software and the remaining 15% was post-corrected after the experiment.

Preparation of electrolyte and product analysis. Preparation of electrolytes and product analysis was performed according to similar procedures reported previously[26].

GCMS analysis of gas and liquid products. The isotopic compositions of both the gas and liquid products were determined using GCMS with an Agilent 7890A GC with a 5975C inert XL MSD (triple axis detector). The column used was an Agilent J&W PoraPLOT Q capillary column of length 25 m, internal diameter 0.25 mm and film thickness 8 µm (part number CP7549). Helium (99.999%) was used as the carrier gas with a flow rate of 1.0 ml min^{-1} in the column. A glass wool liner was used in the inlet, which was set to 250 °C.

For the gas product analysis, 10 µl of gas was injected into the GCMS and the injection mode was split with a 1:1 ratio. For the analysis method, the selected ion monitoring operating mode was used. Elution times of the target analytes (ethylene and ethane) were determined by injecting known standards. During the run, the operating temperature of the oven was set to 30 °C for 7.5 min. A bake out at 100 °C for 5 min was utilized at the end of each run.

For the liquid product analysis, electrolyte samples were first acidified with concentrated hydrochloric acid to pH 2 to convert acetate into the acetic acid form, which is amenable to GCMS analysis. For each analysis, 0.5 µl of sample was injected and the injection mode was split with a 25:1 ratio. The selected ion monitoring operating mode was used for liquid products. Similarly, the elution times of the target analytes (ethanol, 1-propanol and acetic acid) were determined by injecting known standards dissolved in water. During the run, the oven temperature was set to 145 °C for 10 min. A bake out at 200 °C for 5 min was utilized at the end of every run.

To ensure that the mass spectra of different products obtained with our GCMS are consistent with established databases[51], standards of natural isotopic abundances were also injected and all mass fragments with m/z in the range 20 to 75 were scanned (Supplementary Figs. 11–13 give more details).

Determination of the isotopic composition based on the mass spectrometry data is explained in Supplementary Note 4.

^{13}C NMR spectroscopy of liquid products. ^{13}C NMR spectroscopy was utilized to analyse the isotopic composition of the liquid products with a Bruker Avance III 500 MHz spectrometer. The electrolyte with the liquid products (700 µl) was mixed with 35 µl of D_2O that contained 10 mM the electrolyte with the liquid products and 50 mM phenol. To prevent ^{1}H protons from splitting the ^{13}C nuclei, proton decoupling techniques were utilized. Samples were run for at least 12 h to accumulate sufficient signal. Determination of the isotopic composition based on the NMR results is explained in Supplementary Note 5.

Data availability

The data that support the findings of this study are available from the corresponding author upon reasonable request.

Received: 4 July 2018; Accepted: 9 November 2018;
Published online: 17 December 2018

References

1. IPCC *Climate Change 2014: Synthesis Report* (eds Core Writing Team, Pachauri, R. K. & Meyer L. A.) (IPCC, 2014).
2. Chu, S., Cui, Y. & Liu, N. The path towards sustainable energy. *Nat. Mater.* **16**, 16–22 (2017).
3. Hori, Y. Electrochemical CO_2 Reduction on Metal Electrodes. in *Modern Aspects of Electrochemistry* No. 42 (eds Vayenas, C., White, R. & Gamboa-Aldeco, M.) 89–189 (Springer, New York, 2008).
4. Bushuyev, O. S. et al. What should we make with CO_2 and how can we make it? *Joule* **2**, 825–832 (2018).
5. Raciti, D. & Wang, C. Recent advances in CO_2 reduction electrocatalysis on copper. *ACS Energy Lett.* **3**, 1545–1556 (2018).
6. Hori, Y., Murata, A. & Takahashi, R. Formation of hydrocarbons in the electrochemical reduction of carbon dioxide at a copper electrode in aqueous solution. *J. Chem. Soc. Faraday Trans. 1* **85**, 2309 (1989).
7. Kuhl, K. P., Cave, E. R., Abram, D. N. & Jaramillo, T. F. New insights into the electrochemical reduction of carbon dioxide on metallic copper surfaces. *Energy Environ. Sci.* **5**, 7050–7059 (2012).
8. Kuhl, K. P. et al. Electrocatalytic conversion of carbon dioxide to methane and methanol on transition metal surfaces. *J. Am. Chem. Soc.* **136**, 14107–14113 (2014).
9. Li, C. W. & Kanan, M. W. CO_2 reduction at low overpotential on Cu electrodes resulting from the reduction of thick Cu_2O films. *J. Am. Chem. Soc.* **134**, 7231–7234 (2012).
10. Peterson, A. A. et al. How copper catalyzes the electroreduction of carbon dioxide into hydrocarbon fuels. *Energy Environ. Sci.* **3**, 1311–1315 (2010).
11. Cheng, T., Xiao, H. & Goddard, W. A. Reaction mechanisms for the electrochemical reduction of CO_2 to CO and formate on the Cu(100) surface at 298 K from quantum mechanics free energy calculations with explicit water. *J. Am. Chem. Soc.* **138**, 13802–13805 (2016).
12. Garza, A. J., Bell, A. T. & Head-Gordon, M. Mechanism of CO_2 reduction at copper surfaces: pathways to C_2 products. *ACS Catal.* **8**, 1490–1499 (2018).
13. Hori, Y., Takahashi, R., Yoshinami, Y. & Murata, A. Electrochemical reduction of CO at a copper electrode. *J. Phys. Chem. B* **101**, 7075–7081 (1997).
14. Schouten, K. J. P., Qin, Z., Gallent, E. P. & Koper, M. T. M. Two pathways for the formation of ethylene in CO reduction on single-crystal copper electrodes. *J. Am. Chem. Soc.* **134**, 9864–9867 (2012).
15. Kortlever, R., Shen, J., Schouten, K. J. P., Calle-Vallejo, F. & Koper, M. T. M. Catalysts and reaction pathways for the electrochemical reduction of carbon dioxide. *J. Phys. Chem. Lett.* **6**, 4073–4082 (2015).
16. Calle-Vallejo, F. & Koper, M. T. M. Theoretical considerations on the electroreduction of CO to C_2 species on Cu(100) electrodes. *Angew. Chem.* **125**, 7423–7426 (2013).
17. Dinh, C. T. et al. CO_2 electroreduction to ethylene via hydroxide-mediated copper catalysis at an abrupt interface. *Science* **360**, 783–787 (2018).
18. Ma, S. et al. One-step electrosynthesis of ethylene and ethanol from CO_2 in an alkaline electrolyzer. *J. Power Sources* **301**, 219–228 (2016).
19. Peterson, A. A. & Nørskov, J. K. Activity descriptors for CO_2 electroreduction to methane on transition-metal catalysts. *J. Phys. Chem. Lett.* **3**, 251–258 (2012).
20. Hansen, H. A., Varley, J. B., Peterson, A. A. & Nørskov, J. K. Understanding trends in the electrocatalytic activity of metals and enzymes for CO_2 reduction to CO. *J. Phys. Chem. Lett.* **4**, 388–392 (2013).
21. Liu, X. et al. Understanding trends in electrochemical carbon dioxide reduction rates. *Nat. Commun.* **8**, 14580 (2017).
22. Sandberg, R. B., Montoya, J. H., Chan, K. & Nørskov, J. K. CO–CO coupling on Cu facets: coverage, strain and field effects. *Surf. Sci.* **654**, 56–62 (2016).
23. Goodpaster, J. D., Bell, A. T. & Head-Gordon, M. Identification of possible pathways for C–C bond formation during electrochemical reduction of CO_2: new theoretical insights from an improved electrochemical model. *J. Phys. Chem. Lett.* **7**, 1471–1477 (2016).
24. Cheng, T., Xiao, H. & Goddard, W. A. Full atomistic reaction mechanism with kinetics for CO reduction on Cu(100) from ab initio molecular dynamics free-energy calculations at 298 K. *Proc. Natl Acad. Sci. USA* **114**, 1795–1800 (2017).
25. Ma, M., Djanashvili, K. & Smith, W. A. Controllable hydrocarbon formation from the electrochemical reduction of CO_2 over Cu nanowire arrays. *Angew. Chem. Int. Ed.* **55**, 6680–6684 (2016).
26. Lum, Y., Yue, B., Lobaccaro, P., Bell, A. T. & Ager, J. W. Optimizing C–C coupling on oxide-derived copper catalysts for electrochemical CO_2 reduction. *J. Phys. Chem. C* **121**, 14191–14203 (2017).
27. Li, C. W., Ciston, J. & Kanan, M. W. Electroreduction of carbon monoxide to liquid fuel on oxide-derived nanocrystalline copper. *Nature* **508**, 504–507 (2014).
28. Ren, D. et al. Selective electrochemical reduction of carbon dioxide to ethylene and ethanol on copper(I) oxide catalysts. *ACS Catal.* **5**, 2814–2821 (2015).
29. Kas, R., Kortlever, R., Yılmaz, H., Koper, M. T. M. & Mul, G. Manipulating the hydrocarbon selectivity of copper nanoparticles in CO_2 electroreduction by process conditions. *ChemElectroChem* **2**, 354–358 (2014).
30. Raciti, D. et al. Low-overpotential electroreduction of carbon monoxide using copper nanowires. *ACS Catal.* **7**, 4467–4472 (2017).
31. Mistry, H. et al. Highly selective plasma-activated copper catalysts for carbon dioxide reduction to ethylene. *Nat. Commun.* **7**, 12123 (2016).
32. Huang, Y., Handoko, A. D., Hirunsit, P. & Yeo, B. S. Electrochemical reduction of CO_2 using copper single-crystal surfaces: effects of CO* coverage on the selective formation of ethylene. *ACS Catal.* **7**, 1749–1756 (2017).
33. Roberts, F. S., Kuhl, K. P. & Nilsson, A. High selectivity for ethylene from carbon dioxide reduction over copper nanocube electrocatalysts. *Angew. Chem.* **127**, 5268–5271 (2015).
34. Verdaguer-Casadevall, A. et al. Probing the active surface sites for CO reduction on oxide-derived copper electrocatalysts. *J. Am. Chem. Soc.* **137**, 9808–9811 (2015).
35. Feng, X., Jiang, K., Fan, S. & Kanan, M. W. A direct grain-boundary–activity correlation for CO electroreduction on Cu nanoparticles. *ACS Cent. Sci.* **2**, 169–174 (2016).
36. Hahn, C. et al. Engineering Cu surfaces for the electrocatalytic conversion of CO_2: controlling selectivity toward oxygenates and hydrocarbons. *Proc. Natl Acad. Sci. USA* **114**, 5918–5923 (2017).
37. Singh, M. R., Clark, E. L. & Bell, A. T. Effects of electrolyte, catalyst, and membrane composition and operating conditions on the performance of solar-driven electrochemical reduction of carbon dioxide. *Phys. Chem. Chem. Phys.* **17**, 18924–18936 (2015).
38. Xiao, H., Cheng, T., Goddard, W. A. & Sundararaman, R. Mechanistic explanation of the pH dependence and onset potentials for hydrocarbon products from electrochemical reduction of CO on Cu(111). *J. Am. Chem. Soc.* **138**, 483–486 (2016).

39. Resasco, J., Lum, Y., Clark, E., Zeledon, J. Z. & Bell, A. T. Effects of anion identity and concentration on electrochemical reduction of CO_2. *ChemElectroChem* **5**, 1064–1072 (2018).
40. Dutta, A., Rahaman, M., Luedi, N. C., Mohos, M. & Broekmann, P. Morphology matters: tuning the product distribution of CO_2 electroreduction on oxide-derived Cu foam catalysts. *ACS Catal.* **6**, 3804–3814 (2016).
41. Lee, S., Park, G. & Lee, J. Importance of Ag–Cu biphasic boundaries for selective electrochemical reduction of CO_2 to ethanol. *ACS Catal.* **7**, 8594–8604 (2017).
42. Wang, Y. et al. CO_2 reduction to acetate in mixtures of ultrasmall $(Cu)_n$,$(Ag)_m$ bimetallic nanoparticles. *Proc. Natl Acad. Sci. USA* **115**, 278–283 (2018).
43. Ren, D., Ang, B. S.-H. & Yeo, B. S. Tuning the selectivity of carbon dioxide electroreduction toward ethanol on oxide-derived Cu_xZn catalysts. *ACS Catal.* **6**, 8239–8247 (2016).
44. Birdja, Y. Y. & Koper, M. T. M. The importance of Cannizzaro-type reactions during electrocatalytic reduction of carbon dioxide. *J. Am. Chem. Soc.* **139**, 2030–2034 (2017).
45. Calle-Vallejo, F. & Koper, M. T. M. Theoretical considerations on the electroreduction of CO to C_2 species on Cu(100) electrodes. *Angew. Chem. Int. Ed.* 52, 7282–7285 (2013).
46. Singh, M. R., Goodpaster, J. D., Weber, A. Z., Head-Gordon, M. & Bell, A. T. Mechanistic insights into electrochemical reduction of CO_2 over Ag using density functional theory and transport models. *Proc. Natl Acad. Sci. USA* **114**, E8812–E8821 (2017).
47. Cheng, T., Xiao, H. & Goddard, W. A. Nature of the active sites for CO reduction on copper nanoparticles; suggestions for optimizing performance. *J. Am. Chem. Soc.* **139**, 11642–11645 (2017).
48. Pérez-Gallent, E., Marcandalli, G., Figueiredo, M. C., Calle-Vallejo, F. & Koper, M. T. M. Structure- and potential-dependent cation effects on CO reduction at copper single-crystal electrodes. *J. Am. Chem. Soc.* **139**, 16412–16419 (2017).
49. Chen, J. G., Jones, C. W., Linic, S. & Stamenkovic, V. R. Best practices in pursuit of topics in heterogeneous electrocatalysis. *ACS Catal.* **7**, 6392–6393 (2017).
50. Lobaccaro, P. et al. Effects of temperature and gas–liquid mass transfer on the operation of small electrochemical cells for the quantitative evaluation of CO_2 reduction electrocatalysts. *Phys. Chem. Chem. Phys.* **18**, 26777–26785 (2016).
51. Linstrom, P. J. and Mallard, W. G. *NIST Chemistry WebBook* NIST Standard Reference Database Number 69 (National Institute of Standards and Technology, Gaithersburg).

Acknowledgements

This material is based on work performed by the Joint Center for Artificial Photosynthesis, a DOE Energy Innovation Hub, supported through the Office of Science of the US Department of Energy under award no. DE-SC0004993. Y.L. acknowledges the support of an A*STAR National Science Scholarship. We thank A. Buckley for assistance with the ^{13}C NMR spectroscopy and W. R. Leow for assistance with the creation of the figures.

Author contributions

Y.L. and J.W.A. conceived and designed the experiments. Y.L. conducted all the experimental work and analysed the data. Both authors discussed the results and wrote the manuscript.

Competing interests

The authors declare no competing interests.

Additional information

Supplementary information is available for this paper at https://doi.org/10.1038/s41929-018-0201-7.

Reprints and permissions information is available at www.nature.com/reprints.

Correspondence and requests for materials should be addressed to J.W.A.

Publisher's note: Springer Nature remains neutral with regard to jurisdictional claims in published maps and institutional affiliations.